J. Min. Metall. Sect. B-Metall. 62 (1) (2026) 53 - 67

Journal of Mining and Metallurgy, Section B: Metallurgy

A COMPARATIVE STUDY OF MECHANICAL BEHAVIOR OF HEAT-TREATED 3D PRINTED IN-718 AND ASTM F75 ALLOYS ACROSS MULTIPLE LENGTH SCALES

Muhammad Zubair [a,*], Khushnuda Nur [a], Ehsan Ul Haq [a], Furqan Ahmed [a,], Muhammad Adil Javed[b], Muhammad Junaid Khan [a], Muhammad Mubeen Naveed [a], Mirza Mueed ul Hassan [a], Ahmed Abdullah [a]**

[a] Department of Metallurgical and Materials Engineering, Faculty of Chemical, Metallurgical & Polymer Engineering, University of Engineering & Technology (UET), Lahore, Pakistan
[b] IMMESNA, Dubai, UAE

(Received 11 November 2025; Accepted 05 May 2026)

Abstract

The hardness and strength of many alloys often differ when measured at the nano, micro, and macroscopic scales. Therefore, it is essential to study the mechanical behavior of important alloys across a wide range of length scales. In this work, we present a scenario in which two industrially significant alloys, In-718 and ASTM F75, exhibit different behaviors at the micro and macroscopic levels. Both alloys are promising candidates for similar applications in the aerospace and petroleum industries. The alloys were first 3D printed using selective laser melting (SLM) and then heat-treated in a vacuum. The average yield strength and percentage elongation (along the build direction) of the In-718 alloy were 29% and 19% higher, respectively, than those observed for the ASTM F75 alloy. The difference between the ultimate tensile strength (UTS) and Vickers hardness (at a load of 98 N) was almost negligible, i.e., less than 5%. In contrast to the Vickers hardness values of 3.9 GPa and 3.8 GPa, the average nanohardness of the In-718 and ASTM F75 alloys was 5.7 GPa and 7.6 GPa, respectively, which was substantially higher than their Vickers hardness. Furthermore, the ASTM F75 alloy demonstrated much better wear resistance in ScanningWear tests performed using a nanoindenter. The explanation for these differences and the similarities between macro- and nanomechanical behavior are presented in this work.

Keywords: *Mechanical properties; Nanoindentation; Mechanical behavior; Alloys*

1. Introduction

In-718 is a Ni-Fe-Cr-based superalloy renowned for its exceptional mechanical properties and corrosion resistance at room and elevated temperatures up to 650 °C [1]. This alloy derives its strength from the solid solution strengthening and precipitation hardening [1, 2]. Solid solution strengthening of the matrix phase (generally designated as γ phase) in In-718 alloy is attributed to refractory elements such as Mo, Nb, W, and Re [2]. The main precipitation strengthening phases in In-718 alloy are γ′ (Ni_3(Al,Ti)) and γ′′ (Ni_3(Nb,V)) [1-3]. These precipitates are induced in the In-718 alloy by aging treatment preceded by solution treatment process. Full potential of alloying elements in In-718 alloy might not be attained if the elements precipitates as other phases such δ (Ni_3Nb) or Laves phases (Ni, Cr, Fe)$_2$(Nb, Ti, Mo) [4]. This alloy finds many structural applications in aerospace, automobile, and energy sectors [2].

Co-Cr-Mo based alloys (ASTM F75) are well-known for their excellent mechanical properties including wear resistance, biocompatibility, and corrosion resistance [5-9]. The matrix of Co-Cr-Mo alloy generally has two crystal structures: the γ-phase which is FCC and stable at high temperatures or the ε-phase which is HCP and stable at low temperatures. Heat treatment at high temperatures ≈ 1050 °C and subsequent cooling to room temperature usually results in the development of γ-phase even at room temperature. This is because the γ→ε conversion is slow [6]. Further, the matrix phase is reinforced with carbide phases such as $M_{23}C_6$ [10, 11] and M_6C [10]. This alloy is commonly used in biomedical applications, gas turbines, and high temperature applications [7, 12].

The mechanical properties including hardness and wear resistance are crucial for both In-718 and ASTM F75 alloys to be used in the above-mentioned

Corresponding authors: zubair@uet.edu.pk [*]; furqan.ahmed@uet.edu.pk [**]

https://doi.org/10.2298/JMMB251111005Z

applications. Many alloy systems tend to show a phenomenon named as indentation size effect (ISE) in nanoindentation [4, 13-17]. ISE refers to the increase in hardness of the material with decreasing indents depth. As per Nix and Gao [15], the increase in hardness at small depths is attributed to the increased density of geometrically necessary dislocations (GNDs) required to accommodate large plastic strain gradients at small indentation depths. The increased density of dislocations leads to more dislocation interactions and high hardness. The density of GNDs and strain gradient decrease with increasing indentation depth thus leading to lower hardness at large depths, i.e., ISE. The mechanical behavior of an alloy can thus be very different at small scales because of the ISE. So, to completely understand the mechanical behavior of an alloy, it is crucial to test them at multiple length scales.

Selective laser melting (SLM) has recently emerged as one of the promising methods to create 3D components from In-718 and ASTM F-75 alloys [2, 4, 6, 8, 18-20]. Selective laser melting (SLM) is a variant of additive manufacturing (AM) or 3D printing and uses laser power to fuse powder bed layers one by one to build 3D components [11, 21]. Complex geometries without any substantial material loss can be built using AM at a low cost [21]. The method is even more attractive for materials such as In-718 and ASTM F-75 (hard and wear resistant) alloys as very little or no machining is required for components made via 3D printing and thus the need for expensive machining tools is limited [21].

Although the mechanical properties of 3D printed In-718 and ASTM F-75 alloys have been well reported individually [2, 6, 11, 22-25], direct comparisons of their mechanical properties using similar testing techniques are rare. This comparison is important for materials selection in applications where both alloys are the promising candidates such as impellers and sleeves in petroleum industry and gas turbines in aerospace industry. Therefore, in this work, we directly report and compare the mechanical properties of heat-treated 3D printed In-718 and ASTM F75 alloys using similar testing techniques. The mechanical behavior of both alloys is studied over a range of scales using bulk and nanomechanical testing techniques such as tensile testing, Vickers testing, and nanoindentation. The results are interpreted and explained thoroughly in the next sections.

2. Experimental Work

The In-718 and ASTM F75 powders with size distribution of 15-45 μm were used in this study. The laser based additive manufacturing system (Concept laser M2 series 4) was used to build the samples using SLM technique in a vacuum chamber. The process parameters are listed in Table 1.

The composition of In-718 alloy (in wt.%) and ASTM F75 alloy as measured using optical emission spectrometer is given in Table 2.

For microstructural analysis and indentation, cubic samples having dimensions 15 x 15 x 15 mm^3 were printed. For tensile testing, cylindrical coupons with a diameter of 14 mm and a length of 110 mm were first built. These coupons were subsequently machined into dog-bone shaped specimens. Two distinct geometries were produced with gauge lengths of 24 mm and 36 mm. However, the length to diameter ratio of four was maintained in both cases.

As-built In-718 specimens were first subjected to stress-relieving treatment. For this purpose, the specimens were heated to a temperature of 950 °C. The specimens were kept at that temperature for 2 hours and then allowed to cool in the furnace. Stress relieved specimens were then solution annealed at a temperature of 1035 °C for 1.5 hours. The solution-treated specimens were later aged at a temperature of 780 °C for 7 hours. The heating rate in all heat treatment steps was 10 °C/min. Until and unless otherwise mentioned, all treatments were performed in the vacuum furnace. The specimen after solution-treatment and aging were cooled to room temperature through forced gas cooling using Argon (Ar). As-built ASTM F75 specimen were heated at a rate of 10 °C/min to 1050 °C in the vacuum furnace. The specimens were kept at that temperature for 2 hours and then cooled to room temperature using forced Ar gas cooling. Both 3D printing and heat treatment steps

Table 1. *SLM parameters to build 3D In-718 and ASTM F75 specimen*

Printed Material	Laser Spot size (μm)	Laser Power (W)	Scanning rate (mm/s)	Shielding atmosphere	Substrate and its temperature (°C)
In-718	50	370	1000	N_2	SS-316L (0 °C)
ASTM F75	50	210	1250	N_2	SS-316L (80 °C)

Table 2. *Composition of In-718 and ASTM F75 alloy*

Alloy	Ni (%)	Cr (%)	Co (%)	Fe (%)	Mo (%)	Nb (%)	Ti (%)	Al (%)	C (%)
In-718	53.01	18.2	-	18.9	3.11	5.01	0.9	0.61	-
ASTM F75	0.4	27.2	Bal	-	6.22	-	-	0.21	0.13

were performed at Immensa, UAE.

For microstructural analysis, both In-718 and ASTM F75 alloys were first mechanically ground to 2000 SiC emery paper followed by polishing using diamond paste of 6 and 1 µm. Polished In-718 alloy was etched using etchant comprising of 10ml glycerol, 150 ml HCl and 15 ml HNO_3. ASTM F75 alloy, on the other hand, was electrolytically etched using a mixture of 10 ml HCl + 100 ml Distil water. The time, temperature, and voltage were 10 s, 25 °C, and 3 V respectively. Back scattered electron (BSE) imaging in scanning electron microscopy (SEM, Zeiss) was carried out at an accelerating voltage of 15 kV.

All tensile tests were performed at room temperature as per ASTM E8. Vickers indentation was performed at a load of 10 Kg (98 N) at room temperature. Nanoindentation was performed on the polished surface of both alloys with a diamond Berkovich tip using TI Premier Nanoindenter (Bruker). Diamond area function (DAF) of the tip was calibrated on the standard fused quartz sample at ambient temperature using Oliver-Pharr method [26, 27]. The load controlled nanoindentation tests at 10 mN load were performed using low load transducer. The samples were indented at a constant loading rate of 1mN/s up to the maximum load of 10 mN. After a holding time of 2 s, the samples were unloaded at the same rate. The nanoindentation tests at higher loads were done using high load transducers. Loading and unloading rates for high load (> 10 mN) nanoindentation tests were 4 mN/s and -4 mN/s, respectively. Other than that, same calibration procedure and test method was adopted for indents performed at higher loads > 10 mN. All tests were done at room temperature.

The ScanningWear tests were done at ambient temperature on the polished surface of both alloys to determine their wear resistance using the same nanoindenter. Both alloys were raster scanned with a diamond Berkovich tip at a force of 75 µN to produce the wear pattern. A scan consisted of 3 and 5 passes over the same area within the test. The in-situ imaging approach was then used to calculate the amount of material (wear volume) removed during the wear test.

3. Results

3.1. Microstructure and bulk mechanical properties of heat-treated 3D printed In-718 and ASTM F75 alloys

The microstructures of as built and heat-treated In-718 and ASTM F75 alloys are presented in the Figure 1. The as-built microstructure of 3D printed alloys via SLM exhibits a typical fish-scale morphology when viewed along the build direction in the microscope (see Figure 1 a and d) [2, 28, 29]. Heat treatment successfully broke the fish-scale morphology present

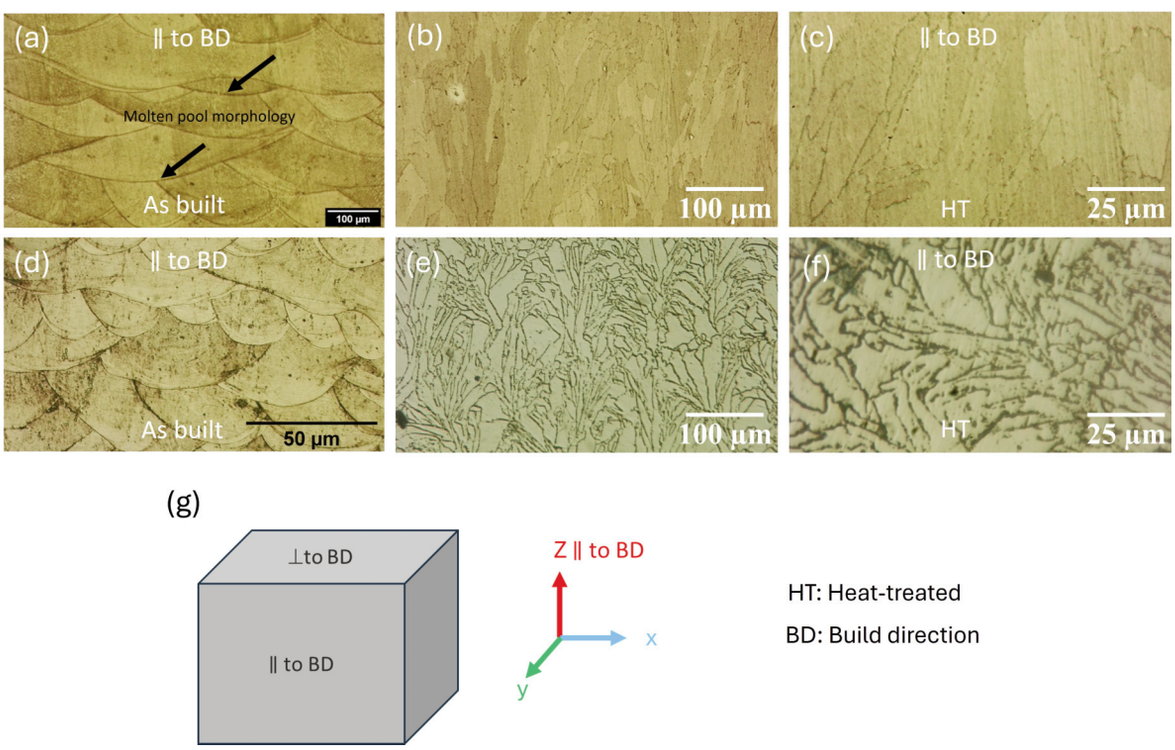

Figure 1. *Microstructures of as built (a) and heat-treated SLM In-718 alloy (b. c); Microstructures of as-cast (d) and heat-treated SLM ASTM F75 alloy (e, f). The polished surfaces visible in the micrographs are || to the BD*

in the as-built specimen of both alloys.

The microstructure of heat-treated In-718 alloy consists of γ matrix enriched with γ′′ precipitates (Figure 2 a and b). In addition, Laves phase precipitates are also present at the grain boundaries (Figure 2 a and b). Similar type of Laves phase morphology was also observed by Shi et al. [30] in their work. Some needle like precipitates, a morphology typically demonstrated by δ phase [31-33], are also present within the γ matrix (Figure 2 b). High hardness and strength of this alloy (see Figure 3, Figure 4 and Figure 5) further compliments their presence.

The microstructure of heat-treated ASTM F75 alloy is dual phase, where solid solution strengthened γ matrix is reinforced with metal carbides (Figure 1 e and f). The white precipitates in the microstructure depict $M_{23}C_6$ precipitates at the grain boundaries (Figure 2 c and d). When these carbides precipitates, they deplete the surrounding region of the Cr, which results in faster corrosion around the carbides and along the grain boundaries [34, 35].

Similar deeply etched regions along the grain boundaries were also visible in the microstructure of the similar alloys [36, 37]. We do not present here, the composition of different phases obtained via energy dispersive spectroscopy (EDS) in SEM, primarily because of the small size of the precipitates. The small size limits the accurate prediction of composition using EDS.

Specifically, the width of Laves phase precipitates in In-718 alloy is ≈ 0.18 ± 0.06 μm, while those of needle-like δ phase have thickness below 100 nm and both length and thickness of disc like γ′′ precipitates is only a few tens of nm (Figure 2) [30, 32]. The carbides in ASTM F75 alloys have an approximate size of 0.8±0.36 μm.

The tensile properties of heat-treated In-718 and Co-Cr alloys are shown in the Figure 3.

In-718 alloy demonstrates higher yield strength and % elongation than the ASTM F75 alloy (see Figure 3). There is no substantial difference between the ultimate tensile strength (UTS) of both alloys, especially when the samples are tested along the build direction.

Overall, for macroscopic specimen In-718 seems to have slightly superior mechanical properties compared to ASTM F75 alloy. The Vickers hardness of In-718 alloy was slightly higher than that of ASTM F75 alloy (see Figure 4).

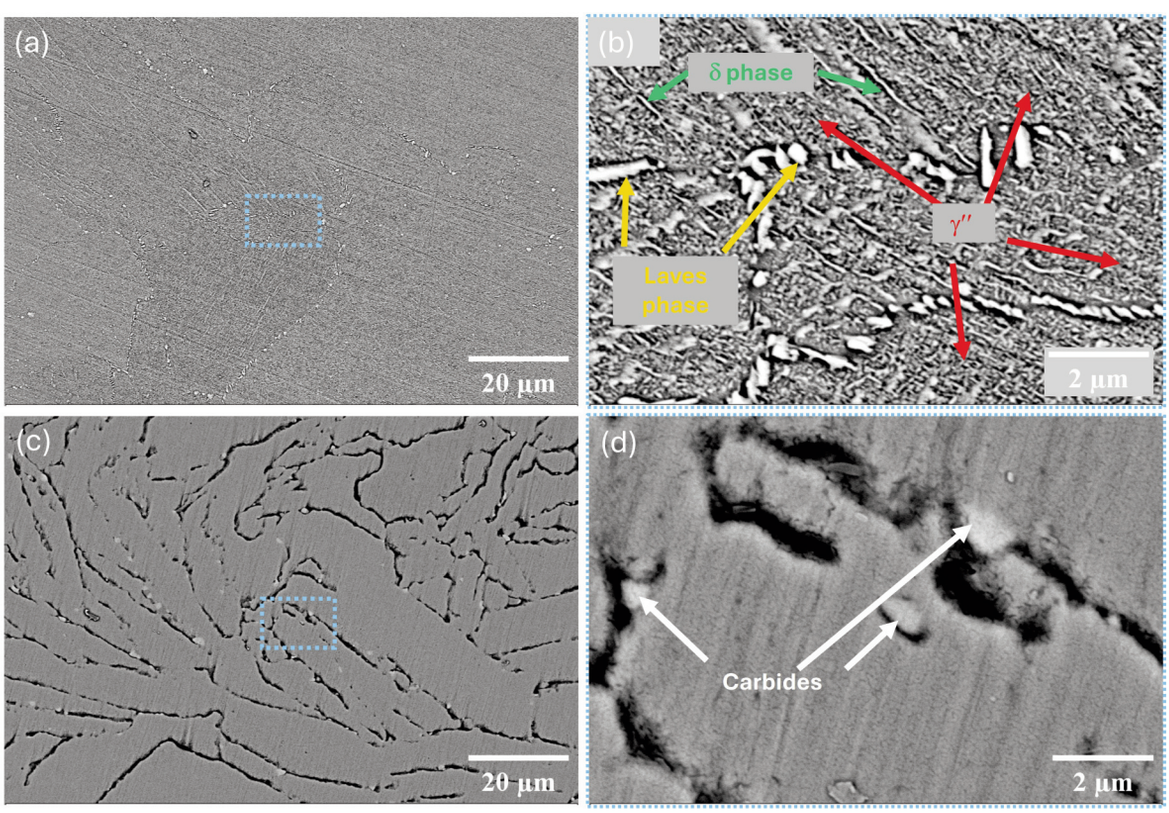

Figure 2. *BSE images of heat-treated In-718 alloy (a, b) and ASTM F75 alloy (c, d). The areas enclosed by blue rectangles in (a) and (c) are depicted in (b) and (d) respectively. Laves phase precipitates in In-718 alloy are highlighted using orange arrows, needle-like δ phase precipitates with green arrows and γ′′ precipitates with red arrows in (b). Metal carbides in F75 alloy are depicted using white arrows in (d)*

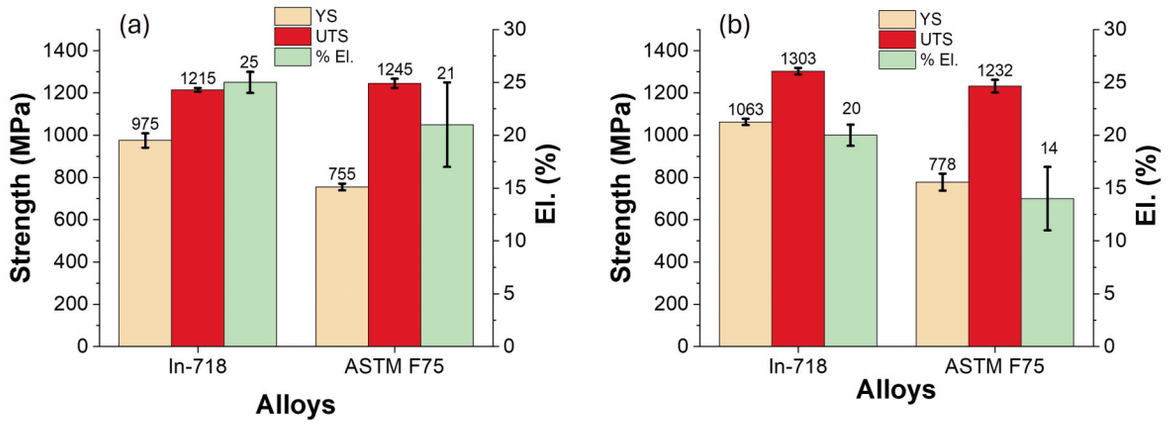

Figure 3. *Tensile properties of In-718 and ASTM 75 (Co-Cr) alloys: (a) parallel to the build direction, (b) perpendicular to the build direction. All tensile tests were performed at room temperature*

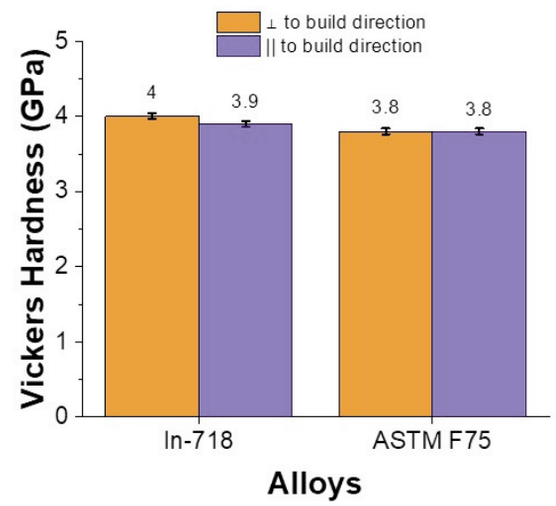

Figure 4. *Vickers hardness of In-718 and Co-Cr alloy at room temperature*

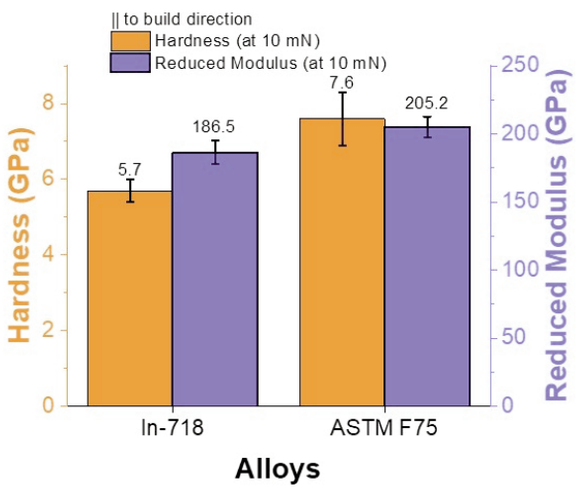

Figure 5. *Hardness and reduced modulus of In-718 and ASTM F75 alloy determined using nanoindentation at ambient temperature*

3.2. Micro and nanomechanical properties of In-718 and ASTM F75 alloys

The hardness trend at small scale was different. In marked contrast to Vickers hardness determined at a load of 98 N, ASTM F75 alloy has a substantially higher hardness than In-718 alloy at a load of 10 mN (see Figure 5).

The scanning wear test revealed that the ASTM F75 alloy had better wear resistance than In-718 alloy. In both 3 and 5 pass tests, the volume removed for In-718 alloy was much more than for ASTM F75 alloy (see Figure 6).

The difference between the hardness of In-718 and ASTM F75 alloy reduced at higher loads (see Figure 7). The difference in hardness of In-718 and ASTM F75 alloy is almost negligible at 200 mN or at contact depth ≈ 1200-1240 nm. This reflects that a more intense size effect exists in ASTM F75 alloy compared to the In-718 alloy.

Indentation size effect (ISE) refers to the increase in hardness of the material with decreasing indents depth. The ISE is caused by the density of geometrically necessary dislocations (GNDs) produced beneath the indenter due to the strain gradient at low displacements [13, 15]. The effect is more prominent at small displacements generally encountered in nanoindentation. Nix-Gao relation can be used to quantify the indentation size effect (see Equation 1) [15]:

$$\frac{H}{H_0} = \sqrt{1 + \frac{h^*}{h}} \tag{1}$$

where H is the hardness of the material at a particular depth, H_0 is the hardness at large depths, h is the contact depth, while h* represents the depth

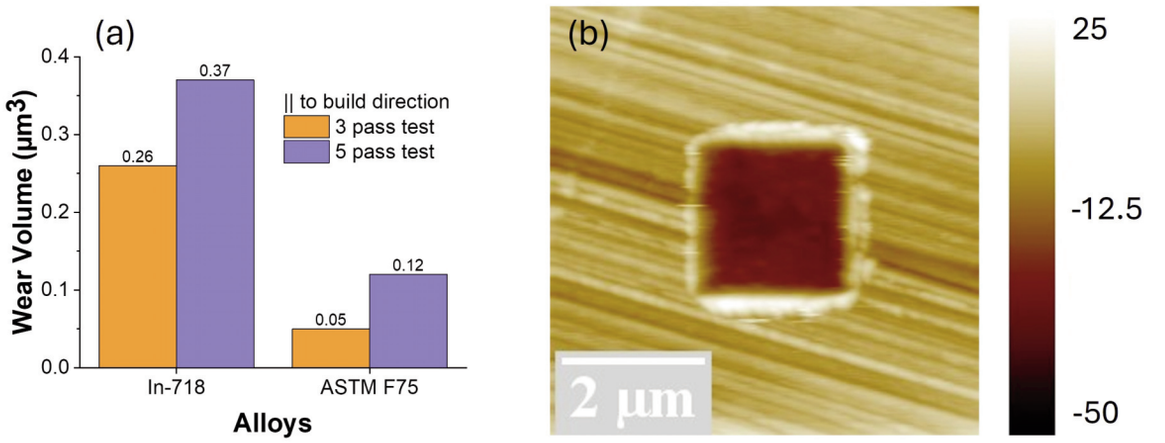

Figure 6. *(a): The volume removed in 3 and 5 pass ScanningWear tests for In-718 and ASTM F75 alloy; (b) Scanning probe microscope (SPM) image of the surface after 5 pass ScanningWear test performed on ASTM F75 alloy*

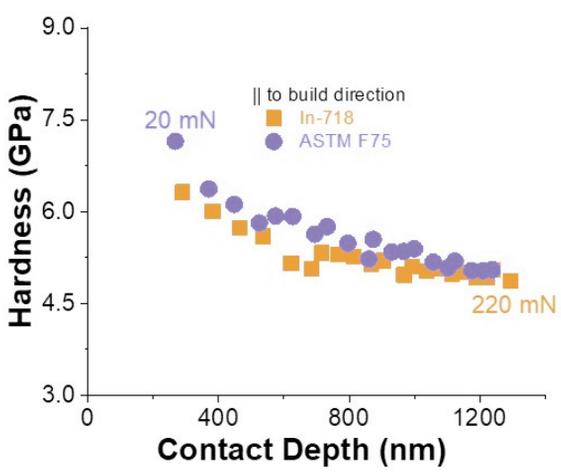

Figure 7. *Variation of hardness as a function of contact depth of In-718 and ASTM F75 alloy. Constant load nanoindentation tests were performed in the load range of 20 mN to 220 mN*

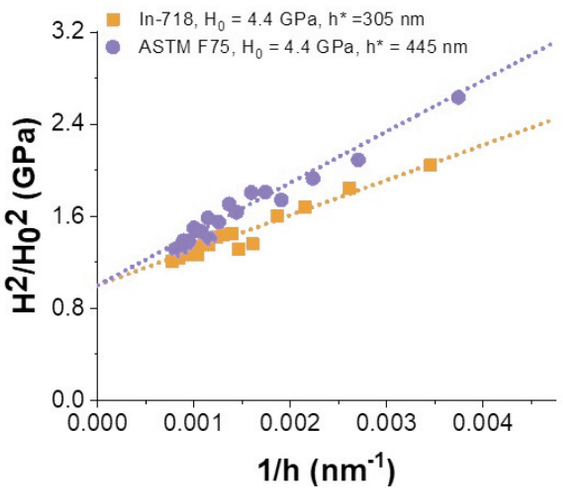

Figure 8. *Fitted curve as per Nix Gao relation for In-718 and ASTM F75 alloy*

below which the size effect is more pronounced [15].

The relationship existing between H^2/H_0^2 and 1/h is shown in Figure 8 for both alloys. H_0 is first calculated using a plot between H and 1/h. It is clear that H_0 values of In-718 and ASTM F75 alloys are quite similar.

Nonetheless, it is clear that a stronger size effect exists for ASTM F75 alloy (see Figure 7 and Figure 8). Furthermore, the characteristic length (h*) beyond which the size effect becomes more prominent for ASTM F75 alloy (431 nm) is ≈ 1.4 times higher than In-718 alloy (305 nm).

The H_0 value calculated for In-718 alloy and ASTM F75 alloys are close to ($H^2/H_0^2 \approx 1.13$ - 1.15) the hardness value determined via Vickers test at a load of 98 N (see Figure 4). This reflects that the data generated via nanoindentation fits well with the Vickers test performed at 98 N.

4. Discussion

4.1. Microstructural evolution and bulk mechanical properties of In-718 alloy and ASTM F75 alloy

Fish-scale morphology in as-built samples is easy to understand by imagining a laser beam creating a molten pool of metallic powder. The metal powder melts and solidifies rapidly in the center of the laser spot due to the presence of highest laser intensity in that region. On either side of the spot, the laser energy distribution is weaker, resulting in a greater degree of metal powder melting in the center and a shallower melting towards the edges [28]. As additional layers are added, these uneven melt zones are stacked on top of each other forming a characteristic fish-scale pattern. The fish-scale morphology is not observed in the heat-treated samples of both alloys: In-718 and ASTM F75. This makes clear that heat treatment has

successfully broken down the fish-scale morphology.

The microstructure of heat treated In-718 alloy is presented in the Figure 1 (b and c). As previously mentioned in section 1, In-718 alloy is a precipitation hardened alloy. The γ′ and γ′′ precipitates are generally induced by the two-stage aging process usually followed by solution treatment at high temperatures [38, 39]. The solution treatment step is essential to dissolve the detrimental Laves phase (Ni, Cr, Fe)$_2$(Nb, Ti, Mo) in the microstructure of as printed alloys. Dissolution of Laves phase is important since it will then release the Nb in the matrix which is a prime element in the γ′ and γ′′ strengthening phases. Temperatures more than 1000 °C are preferred for efficient dissolution of Laves phase in the microstructure [40, 41]. Zhi et al. [40] reported in their work, that Laves phase was almost completely dissolved during solution treatment of In-718 alloy at 1020 °C for 1 hr. Even higher temperatures are recommended by several other authors for complete dissolution of Laves phases in In-718 alloy [30, 38, 41, 42]. In this work, solution treatment temperature of 1035 °C for 1.5 hours was used to dissolve the Laves phase and homogenize the microstructure. Once the microstructure is homogenized and the alloying elements exist in the solid solution then the aging process is used to induce γ′ and γ′′ strengthening phases. Both phases are generally induced by a two-stage aging process consisting of holding solution treated specimen at a temperature of 720 °C for 8 hours followed by slow cooling to 620 °C for 8 hours before air cooling to room temperature [38, 43]. High temperature aging tends to induce the precipitation of γ′′ phase while the low temperature aging is responsible for the γ′ precipitation [43]. The two step aging condition generally results in very high yield (≥ 1100 MPa) and tensile strengths (≥ 1300 MPa) but lower elongations (< 20%). Higher strengths are generally associated with lower ductility (see Table 3) [22, 39, 40, 44]. The applications of In-718 alloy in oil and gas sector do not need very high strength level and hence solution-treatment in between 1010 to 1065 °C followed by single step aging between 650 to 815 °C is enough to achieve desired properties (high toughness, sufficient strength and good corrosion resistance) [45]. This type of heat treatment results in relatively lower strength but appreciable ductility (see Figure 3 and Table 3). Since the components made by Immensa are targeted for oil and gas sector so the single step aging treatment was used. Thus, the microstructure of heat treated In-718 (Figure 2 a and b) consists primarily of γ matrix reinforced with nm sized γ′′ particles. In addition to that Laves phase precipitates, some amount of needle like δ-phase is also present within the γ matrix (see Figure 2) [46]. Furthermore, the regions around needle-like intragranular δ-precipitates are free of nm sized γ′′ precipitates.

The microstructure of heat-treated ASTM F75 alloy is presented in Figure 1 (e and f) and Figure 2 (c and d). The alloy was heat treated at 1050 °C for 2 hours before being quenched to room temperature using forced Ar. The matrix of ASTM F75 alloy consists of γ phase in such situations [6]. The Co-Cr-Mo containing γ-matrix exhibits better elongation, but lower hardness and strength compared with the same alloys heat-treated at lower temperature (< 920°C, below the γ→ε transformation temperature) and containing e phase or a combination of γ and ε phases (Table 4) [6, 48]. The γ→ε conversion is very slow and requires an isothermal aging treatment below the transformation temperature for completion [6, 49]. The metastable γ phase, retained by fast cooling, can be converted into ε phase via strain induced martensitic transformation (SIMT) [50]. SIMT is also the main deformation mechanism of this alloy and influences the ductility and work hardening capabilities of this alloy [51]. Further, carbides ($M_{23}C_6$ [10, 11] and M_6C [10], where M is Cr, Mo, Co) are present as a reinforcement phase in the microstructure (Figure 1 e and f, Figure 2 c and d) [6, 37]. The carbides usually exist at the grain boundaries and interdendritic regions in 3D printed alloys and may also be present in the heat-treated alloys at the grain boundaries [34, 36, 37, 52]. To completely dissolve carbides a solution treatment temperature of ≈ 1200 °C for several hours is recommended [53, 54]. A solution treatment temperature of 1050 °C and time of 2 hours used in this study was not enough to completely dissolve the carbides phase. So, these could be observed in the solution treated microstructures presented in Figure 2 (c and d).

As mentioned, ASTM F75 alloy is primarily strengthened with solid solution strengthening induced by Cr and Mo and carbide strengthening because of the presence of various types of carbides [52, 55]. $M_{23}C_6$ type carbides are typically Cr rich while M_6C type carbides are Mo rich [37, 52]. Apart from that the alloying elements also tend to form an oxide layer on the surface of the ASTM F75 alloy. An oxide layer of 1.8 nm comprising mainly of Cr_2O_3 was immediately formed on the surface of Co-Cr-Mo alloy when it was exposed to air [56]. In this work, the alloy consisted of a γ-phase reinforced with metal carbides, so it demonstrated appreciable ductility (due to the γ-phase) as well as high yield and tensile strength (because of metal carbides, see Figure 3 and Table 4). A large scatter was observed in the % elongation for ASTM F75 alloy and this can very well be attributed to the presence of carbides along the grain boundaries of g matrix. These carbides can act as a preferential source of cracks nucleation and their slight inhomogeneous distribution across the γ matrix can thus influence the ductility in differently in various

Table 3. *Comparison of mechanical properties of In-718 alloy developed using different synthesis routes*

Ref.	Synthesis route of In-718 alloy	Treatment	Hardness, H_v (GPa)	Yield Strength, MPa	UTS, MPa	Elongation, %
[22]	Constant laser power deposition	ST^1: 980 °C/1 h; DA^2: 720 °C/8 h, 620 °C/8 h	427 (≈4.2)	≈1104	≈1392	≈11
	Gradient laser power deposition	ST^1: 980 °C/1 h; DA^2: 720 °C/8 h, 620 °C/8 h	446 (≈4.4)	≈1196	≈1430	≈10
	Constant laser power deposition	Homogenization: 1100 °C/1.5 h; ST^1: 980 °C/1 h; DA^2: 720 °C/8 h, 620 °C/8 h	443 (≈4.3)	≈1189	≈1322	≈13
	Gradient laser power deposition	Homogenization: 1100 °C/1.5 h; ST^1: 980 °C/1 h; DA^2: 720 °C/8 h, 620 °C/8 h	446 (≈4.4)	≈1298	≈1443	≈12
[39]	Laser solid forming (1350 W)	ST^1: 1100 °C/1.5 h	239 (≈2.3)	≈340	≈756	≈61
	Laser solid forming (1350 W)	Homogenization: 1100 °C/1.5 h; ST^1: 980 °C/1 h; DA^2: 720 °C/8 h, 620 °C/8 h	496 (≈4.9)	≈1129	≈1342	≈16
[40]	Selective laser melting (LSM)	ST^1: 960 °C/1 h; DA^2: 720 °C/8 h, 620 °C/8 h	≈431 (≈4.2)	≈1154	≈1215	≈18
		ST^1: 980 °C/1 h; DA^2: 720 °C/8 h, 620 °C/8 h	≈442 (≈4.3)	≈1231	≈1290	≈17
		ST^1: 1000 °C/1 h; DA^2: 720 °C/8 h, 620 °C/8 h	≈452 (≈4.4)	≈1351	≈1396	≈16
		ST^1: 1020 °C/1 h; DA^2: 720 °C/8 h, 620 °C/8 h	≈437 (≈4.3)	≈1330	≈1374	≈17
[44]	Selective laser melting (LSM)	Homogenization: 1100 °C/1.5 h; ST^1: 980 °C/1 h; DA^2: 720 °C/8 h, 620 °C/8 h	≈461 (≈4.5)	≈1102	≈1362	≈13
		ST^1: 980 °C/1 h; DA^2: 720 °C/8 h, 620 °C/8 h	≈482 (≈4.7)	≈1173	≈1384	≈11
		DA^2: 720 °C/8hr, 620 °C/8hr	≈427 (≈4.2)	≈1047	≈1251	≈12
[42]	Laser directed energy deposition	DA^2: 720 °C/10 h, 620 °C/10 h	≈395 (≈3.9)	≈995	≈1245	≈17
		Single aging: 850 °C/4 h	≈344 (≈3.4)	≈645	≈1043	≈27
		ST^1: 1100 °C/1 h; DA^2: 760 °C/10 h, 650 °C/10 h	≈412 (≈4.0)	≈990	≈1249	≈22
		ST^1: 1100 °C/1 h; Single aging: 760 °C/10 h	≈378 (≈3.7)	-	-	-
		ST^1: 1100 °C/1 h; Single aging: 760 °C/20 h	≈363 (≈3.6)	-	-	-
		ST^1: 1100 °C/1 h; Single aging: 650 °C/10 h	≈413 (≈4.0)	-	-	-
		ST^1: 1100 °C/1 h; Single aging: 650 °C/20 h	≈413 (≈4.0)	≈1005	≈1247	≈23
[47]	Selective laser melting (SLM)	ST^1: 1080 °C/1 h; Single aging: 650 °C/20 h	-	≈989	≈1342	≈23
		ST^1: 1080 °C/1 h; Single aging: 750 °C/20 h	-	≈1080	≈1410	≈25
		ST^1: 1080 °C/1 h; Single aging: 850 °C/20 h	-	≈870	≈1250	≈31%
This work	Selective laser melting (SLM)	SR^3: 950 °C/2 h	≈410 (≈4)	≈975	≈1215	≈25
		ST^1: 1035 °C/1.5 h;				
		Single aging: 780 °C/7 h				

ST^1 refers to solution treatment, while DA^2 and SR^3 depict double aging and stress relieving, respectively.

Table 4. *Comparison of mechanical properties of In-718 alloy developed using different synthesis routes*

Ref.	Synthesis route of Co-28Cr-6Mo alloy (ASTM F75)	Treatment	Hardness, H_v (GPa)	Yield Strength, MPa	UTS, MPa	Elongation, %
[6]	Selective laser melting (SLM)	HT*: 750 °C /2 h	≈487 (≈4.8)	≈1048	≈1102	≈4
[6]		HT: 1050 °C/ 2 h	≈487 (≈4.8)	≈690	≈1014	≈26
[11]	Selective laser melting (SLM)	Preheating: 815 °C/4 h, ST: 1220 °C/1 h	≈298 (≈2.9)	≈450	≈630	≈14
		ST: 1220 °C/2 h	≈302 (≈3.0)	≈415	≈530	≈13
		ST: 1220 °C/4 h	≈333 (≈3.3)	≈410	≈530	≈20
[51]	Laser powder bed fusion	ST: 1150 °C/1 h	≈343 (≈3.4)	≈405	≈980	≈32
		HT: 750°C/2 h	≈439 (≈4.3)	≈945	≈1195	≈11
		ST: 1150 °C/1 h, Aging: 750°C/2 h	≈334 (≈3.3)	≈663	≈1122	≈24
[48]	Selective laser melting (SLM)	HT: 1200 °C/2 h	≈486 (≈4.8)	≈846	≈1001	≈12
		HT: 1200 °C/1 h	≈455 (≈4.5)	≈620	≈873	≈18
This work	Selective laser melting (SLM)	HT: 1050 °C /2 h	≈391 (≈3.8)	≈755	≈1245	≈24

HT: heat-treated*

samples. Additionally, strain induced transformation of γ→ε results in the formation of γ/ε interfaces. The strain may accumulate at these interfaces resulting in the nucleation of cracks during plastic deformation [51]. Such heterogeneous materials generally exhibit a relatively large scatter in their %elongation values and was also observed by Tham et al. [42], Sing et al. [11] and Im et al. [6] in their work on similar alloys.

If the macro mechanical properties of the two alloys are compared along the BD, the In-718 alloy exhibited a ≈ 29% higher yield strength (975 MPa) than the ASTM F75 alloy (755 MPa). While the tensile strength of In-718 (1215 MPa) was ≈ 2% lower compared to ASTM F75 alloy (1245 MPa), it demonstrated a 19% higher elongation (25% vs 21%) and a 3% more Vickers hardness (3.9 GPa vs 3.8 GPa).

4.2. Micro and nanomechanical properties of In-718 and ASTM F75 alloys

Although hardness of In-718 alloy was ≈3% higher than ASTM F75 alloy at macroscopic level, the results were very different at small scale. The nano-hardness of In-718 alloy (5.7 GPa) at a load of 10mN was ≈ 25 % lower than the average nano-hardness of ASTM F75 alloy (7.6 GPa, see Figure 4, Figure 5, and Figure 9). Moreover, the observed nano-hardness (at 10mN) of In-718 alloy (5.7 GPa) was ≈ 46% higher than the Vickers hardness (3.9 GPa at ≈ 98N). On the other hand, the nano-hardness of ASTM F75 alloy (7.6 GPa) was ≈ 100% higher than the macroscopic hardness (3.8 GPa). This reflects that both In-718 and ASTM F75 alloy show an ISE and by varying amounts. A substantial difference between nano and Vickers hardness was also reported by Patel et al. [57] for ASTM F75 alloy. Furthermore, much higher scatter was observed in nano-hardness for ASTM F75 alloy primarily because the size of reinforcement phase (carbides) is bigger. Since carbides have very high hardness [57] so any indent placed closer to the carbide phase or partially on the carbide phase is expected to have much higher hardness values.

The ScanningWear tests using nanoindenter also revealed that the volume lost due to wear at the same load was 3-5 times more for In-718 alloy than the ASTM F75 alloy. The whole information is summarized in Figure 9.

This demonstrates substantial wear resistance of

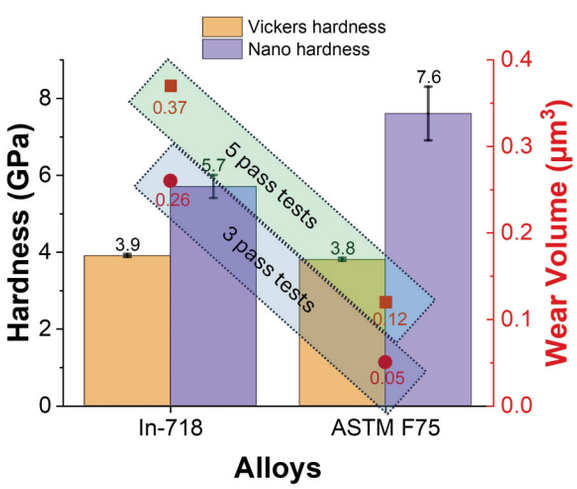

Figure 9. *Comparison of Vickers and nano hardness of In-718 and ASTM F-75 alloy. The wear volume in 3 and 5 pass ScanningWear tests is superimposed on the bar charts for both alloys*

ASTM F75 alloy compared to In-718 alloy. Generally higher hardness is associated with better wear resistance and in this context the results of nano-hardness and wear resistance complement each other. The test was conducted at a load of 75 μN and the depth to which indenter penetrated was limited to only a few tens of nm. As described in the previous section, there is Cr_2O_3 layer almost always present on the surface of ASTM F75 alloy. This layer has very high hardness [57] and is most probably responsible for high wear resistance of ASTM F75 alloy at small scales. The volume loss due to wear of In-718 in 3-pass and 5-pass tests was 0.26 and 0.37 μm^3. The respective values of volume loss for ASTM F75 alloy were 0.05 and 0.12 μm^3. Thus, the percentage difference between the volume loss due to wear of In-718 alloy and ASTM F75 alloy decreased by almost 2 times (≈ 3 times) in a 5-pass wear test compared to (≈ 5 times) in a 3-pass test. This indicates that the influence of oxide layer on wear performance decreases as the indenter penetrates deeper in the material.

4.3. Size effect in In-718 and ASTM F75 alloys

The In-718 and ASTM F75 alloys have very high nano-hardness as compared to their hardness at high loads (see section 4.2). The extent of increase is different for both alloys. To examine this in more detail, more nanoindentation experiments were then performed over a range of load using high load transducer. It is evident that the hardness of In-718 and ASTM F75 alloys decreases with increasing load (see Figure 7). Furthermore, at higher loads, the difference between the hardness of both alloys reduces and there is almost no difference in hardness values beyond the load of 200 mN or contact depths of ≈1200 nm. The ISE is thus much more intense and h* is ≈ 40% higher for ASTM F75 (h* ≈ 431 nm) alloy compared to the In-718 (h* ≈ 305 nm).

4.4. Comparison of small scale and bulk deformation of both alloys

Plastic deformation in tensile test at bulk scale can be well described using Hollomon equation (see Equation 2 [58]):

$$\sigma = K \cdot \varepsilon^n \tag{2}$$

Here, σ represents flow stress, K is the strength coefficient, ε is true strain and n is the strain hardening exponent. Higher value of n indicates more strain hardening due to increased dislocation interactions. The values of K, n, and $S_{UTS} - S_{0.2}$ (ultimate tensile strength-yield strength) are summarized in the Figure 10.

While the In-718 alloy has better yield strength, the ASTM F75 alloy has a higher strain hardening exponent (n ≈ 0.16 vs 0.11) and strength coefficient (K ≈ 1928 vs 1708). Since K represents the value of true stress when true strain is 1, so this means the higher value will indicate a stronger material. The strain hardening occurs in the material because of dislocation interactions. Higher dislocation density leads to more dislocation interactions and thus higher strain hardening exponents.

As mentioned in section 1, the ISE is generally associated with steeper strain gradients developed underneath an indenter especially at low depths. The strain gradients then produce many GNDs. This increases the dislocation density, and their interaction leads to high hardness at low depths. The h* refers to that depth below which the ISE would become prominent because of GNDs.

Strain hardening exponent, n, calculated in this work is from bulk tensile test. It has been shown in many earlier studies that microstructures containing inhomogeneities such as grain boundaries, phase boundaries, and cracks can often lead to strain gradients at microstructural level [59-64]. The strain gradients can thus create GNDs which increases the density of dislocations and their interactions and high strain or work hardening [64]. In ASTM F75 alloy having γ matrix, strain may induce ε transformation. High strain partitioning at the γ/ε interfaces during the plastic deformation, requires the generation of large number of GNDs as well [51]. The materials generating higher density of GNDs will have more n value which is generally determined from the tensile test and h* value calculated from nanoindentation tests over a range of depths. The same is observed in this work, where ASTM F75 alloy has higher h* and n values compared to In-718 alloy.

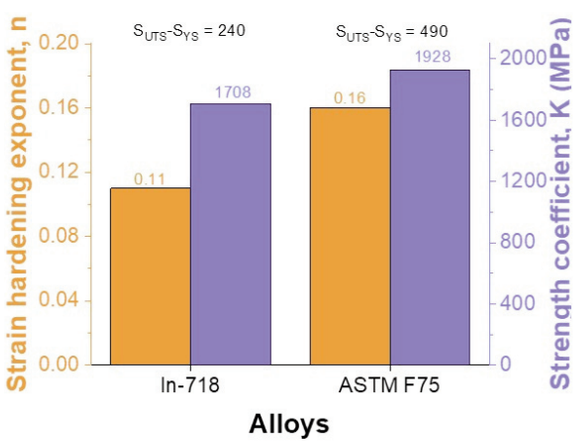

Figure 10. *Comparison of strain hardening exponent (n), strength coefficient (K) and ultimate tensile strength (S_{UTS})- yield strength (S_{YS}) values for both In-718 and ASTM F75 alloy*

5. Conclusions

In this work, we studied the mechanical behavior of In-718 and ASTM F75 alloys over a range of length scales. Both alloys were first 3D printed using SLM technique and then were heat-treated in vacuum.

- The heat-treated microstructure of the In-718 alloy consists of a γ matrix reinforced primarily with γ′′ precipitates. The heat-treated microstructure of the ASTM F75 alloy consists of a γ matrix reinforced with interconnected carbides.
- The average yield strength, UTS, and % elongation, when determined along BD, of the In-718 alloy were 975 MPa, 1215 MPa, and 25%, respectively, for the In-718 alloy. The same values for the ASTM F75 alloy were 755 MPa, 1245 MPa, and 21%.
- The average Vickers' hardness (at a load of ≈ 98 N) for the In-718 and the ASTM F75 alloys were 3.9 and 3.8 GPa, respectively. These values indicate that the mechanical properties of the In-718 alloy are comparable, in fact better, than the ASTM F75 alloy at bulk scale.
- The average nano-hardness at a load of 10 mN were 5.7 GPa and 7.6 GPa for the In-718 alloy and the ASTM F75 alloy, respectively.
- The volume removed during ScanningWear tests was 3 to 5 times more for the In-718 alloy indicating better wear resistance of the ASTM F75 alloy. These results indicate that an ISE of variable magnitude is shown by both alloys. The characteristic lengths (h*) determined for the In-718 and ASTM F75 alloys were 305 nm and 431 nm, respectively.
- The h* values calculated from nanoindentation experiments and strain hardening exponent (n) values calculated from bulk tensile tests, indicates that the role of GNDs is more pronounced in the ASTM F75 alloy than the In-718 alloy.

The study thus highlights the importance of studying the mechanical behavior over a wide length scale: from nano to macro level.

Acknowledgements

We are very grateful to Mr. Muhammad Mateen and Mr. Inderias Barkat for their help in the sample preparation for microscopic analysis. We are also thankful to Dr. Muhammad Ramzan Abdul Karim for his help in doing SEM.

Author's contributions

Muhammad Zubair: Conceptualization, Methodology, Validation, Formal analysis, Investigation, Resources, Data Curation, Writing - Original Draft, Writing-Review & Editing, Visualization, Supervision; Khushnuda Nur: Validation, Formal analysis, Investigation, Resources, Data Curation, Writing - Review & Editing, Visualization; Ehsan ul Haq: Validation, Formal analysis, Investigation, Writing - Review & Editing, Visualization; Furqan Ahmed: Validation, Formal analysis, Investigation, Resources, Writing - Review & Editing, Visualization, Supervision; Muhammad Adil Javed: Methodology, Investigation, Validation, Resources; Muhammad Junaid Khan: Methodology, Investigation, Formal Analysis; Muhammad Mubeen Naveed: Methodology, Investigation, Formal Analysis; Mirza Mueed ul Hassan: Methodology, Investigation; Ahmed Abdullah: Methodology, Investigation.

Data availability

Data may be made available upon reasonable request.

Conflict of interest

There is no known conflict of interest.

References

[1] T. Sonar, V. Balasubramanian, S. Malarvizhi, T. Venkateswaran, D. Sivakumar, An overview on welding of Inconel 718 alloy - Effect of welding processes on microstructural evolution and mechanical properties of joints, Materials Characterization, 174 (2021) 110997. https://doi.org/10.1016/j.matchar.2021.110997

[2] M. Shahwaz, P. Nath, I. Sen, A critical review on the microstructure and mechanical properties correlation of additively manufactured nickel-based superalloys, Journal of Alloys and Compounds, 907 (2022) 164530. https://doi.org/10.1016/j.jallcom.2022.164530

[3] H.K.D.H. Bhadeshia, Nickel Based Superalloys, Available at: https://www.phase-trans.msm.cam.ac.uk/2003/Superalloys/superalloys.html

[4] H. Wang, A. Dhiman, H.E. Ostergaard, Y. Zhang, T. Siegmund, J.J. Kruzic, V. Tomar, Nanoindentation based properties of Inconel 718 at elevated temperatures: A comparison of conventional versus additively manufactured samples, International Journal of Plasticity, 120 (2019) 380-394. https://doi.org/10.1016/j.ijplas.2019.04.018

[5] M. Choi, H. Lee, Y. Song, J. Kim, J. Gwon, H. N. Han, B. Lee, Correlation between microstructures and mechanical properties in directly deposited Co-Cr-Mo alloys with line energies, Materials Characterization, 213 (2024) 113994. https://doi.org/10.1016/j.matchar.2024.113994

[6] H.-T. Im, D.H. Kim, Y.D. Kim, J.O. Fadonougbo, C.B. Mo, J.-Y. Park, K.B. Park, J.-W. Kang, H.-S. Kang, H.-K. Park, Effect of phase transformation on the mechanical properties of the Co-Cr-Mo alloy fabricated by selective laser melting, Materials Characterization, 186 (2022) 111767. https://doi.org/10.1016/j.matchar.2022.111767

[7] J. Quintero-Ortiz, F.V. Guerra, A. Bedolla-Jacuinde, C. A. Leon-Patiño, J.S. Pacheco-Cedeño, Sliding wear behavior of Co-Cr-Mo alloys with C and B additions for wear applications, Wear, 522 (2023) 204698. https://doi.org/10.1016/j.wear.2023.204698

[8] M. Atapour, S. Sanaei, Z. Wei, M. Sheikholeslam, J.D. Henderson, U. Eduok, Y. K. Hosein, D.W. Holdsworth, Y.S. Hedberg, H.R. Ghorbani, In vitro corrosion and biocompatibility behavior of CoCrMo alloy manufactured by laser powder bed fusion parallel and perpendicular to the build direction, Electrochimica Acta, 445 (2023) 142059. https://doi.org/10.1016/j.electacta.2023.142059

[9] K. Zhou, J. Chen, T. Wang, Y. Su, L. Qiao, Y. Yan, Effect of surface energy on protein adsorption behaviours of treated CoCrMo alloy surfaces, Applied Surface Science, 520 (2020) 146354. https://doi.org/10.1016/j.apsusc.2020.146354

[10] J.V. Giacchi, O. Fornaro, H. Palacio, Microstructural evolution during solution treatment of Co–Cr–Mo–C biocompatible alloys, Materials Characterization, 68 (2012) 49-57. https://doi.org/10.1016/j.matchar.2012.03.006

[11] S.L. Sing, S. Huang, W.Y. Yeong, Effect of solution heat treatment on microstructure and mechanical properties of laser powder bed fusion produced cobalt-28chromium-6molybdenum, Materials Science and Engineering: A, 769 (2020) 138511. https://doi.org/10.1016/j.msea.2019.138511

[12] G. Cui, H. Liu, S. Li, G. Gao, M. Hassani, Z. Kou, Effect of Ni, W and Mo on the microstructure, phases and high-temperature sliding wear performance of CoCr matrix alloys, Science and Technology of Advanced Materials, 21 (1) (2020) 229-241. https://doi.org/10.1080/14686996.2020.1752113

[13] O. Franke, J.C. Trenkle, C.A. Schuh, Temperature dependence of the indentation size effect, Journal of Materials Research, 25 (7) (2010) 1225-1229. https://doi.org/10.1557/JMR.2010.0159

[14] V. Maier, C. Schunk, M. Göken, K. Durst, Microstructure-dependent deformation behaviour of bcc-metals – indentation size effect and strain rate sensitivity, Philosophical Magazine, 95 (16-18) (2015) 1766-1779. https://doi.org/10.1080/14786435.2014.982741

[15] W.D. Nix, H. Gao, Indentation size effects in crystalline materials: A law for strain gradient plasticity, Journal of the Mechanics and Physics of Solids, 46 (3) (1998) 411-425. https://doi.org/10.1016/S0022-5096(97)00086-0

[16] M. Zubair, S. Sandlöbes-Haut, M. Lipińska-Chwałek, M.A. Wollenweber, C. Zehnder, J. Mayer, J.S.K.L. Gibson, S. Korte-Kerzel, Co-deformation between the metallic matrix and intermetallic phases in a creep-resistant Mg-3.68Al-3.8Ca alloy, Materials & Design, 210 (2021) 110113. https://doi.org/10.1016/j.matdes.2021.110113

[17] P. Wang, Y. Gao, P. Wang, A comparative study of indentation size effect models for different materials, Scientific Reports, 14 (1) (2024) 20010. https://doi.org/10.1038/s41598-024-71136-5

[18] R. Jiang, A. Mostafaei, Z. Wu, A. Choi, P.-W. Guan, M. Chmielus, A.D. Rollett, Effect of heat treatment on microstructural evolution and hardness homogeneity in laser powder bed fusion of alloy 718, Additive Manufacturing, 35 (2020) 101282. https://doi.org/10.1016/j.addma.2020.101282

[19] S. Naskar, S. Suryakumar, B.B. Panigrahi, Heat treatments effects on wear performance of laser based powder bed dusion fabricated Inconel 718 alloy, Wear, 556-557 (2024) 205526. https://doi.org/10.1016/j.wear.2024.205526

[20] V.K.A, P. K.R, H.P, J.K. Katiyar, S.K, Advancements in laser powder bed fusion manufacturing of Alloy 718: Microstructural insights and mechanical behaviours, Journal of Alloys and Compounds, 1037 (2025) 182631. https://doi.org/10.1016/j.jallcom.2025.182631

[21] M.E. Korkmaz, M.K. Gupta, G. Robak, K. Moj, G.M. Krolczyk, M. Kuntoğlu, Development of lattice structure with selective laser melting process: A state of the art on properties, future trends and challenges, Journal of Manufacturing Processes, 81 (2022) 1040-1063. https://doi.org/10.1016/j.jmapro.2022.07.051

[22] L. Xu, Z. Chai, B. Peng, W. Zhou, X. Chen, Effect of heat treatment on microstructures and mechanical properties of Inconel 718 additively manufactured using gradient laser power, Materials Science and Engineering: A, 868 (2023) 144754. https://doi.org/10.1016/j.msea.2023.144754

[23] M. Švec, P. Solfronk, I. Nováková, J. Sobotka, J. Moravec, Comparison of the structure, mechanical properties and effect of heat treatment on alloy Inconel 718 produced by conventional technology and by additive layer manufacturing, Materials, 16 (15) (2023) 5382. https://doi.org/10.3390/ma16155382

[24] H. Deng, Y. Wang, L. Lv, S. Zhang, Q. Bian, J. Luo, Z. Wu, Z. Liu, Z. Chen, L. Tan, F. Liu, Orientation dependence of microstructure and mechanical property in selective laser-melted Inconel 718 alloy, Materials Characterization, 220 (2025) 114664. https://doi.org/10.1016/j.matchar.2024.114664

[25] S.N. Emmanouilidou, A.G. Lekatou, A.D. Papagiannopoulos, Z.Z. Siaraka, I.E. Tzala, Effect of Nb low-alloying on the microstructure, corrosion and wear performance of a Co-28Cr-6Mo alloy fabricated by vacuum arc melting, International Journal of Refractory Metals and Hard Materials, 133 (2025) 107330. https://doi.org/10.1016/j.ijrmhm.2025.107330

[26] W.C. Oliver, G.M. Pharr, Measurement of hardness and elastic modulus by instrumented indentation: Advances in understanding and refinements to methodology, Journal of Materials Research, 19 (1) (2004) 3-20. https://doi.org/10.1557/jmr.2004.19.1.3

[27] W.C. Oliver, G.M. Pharr, An improved technique for determining hardness and elastic modulus using load and displacement sensing indentation experiments, Journal of Materials Research, 7 (6) (1992) 1564-1583. https://doi.org/10.1557/JMR.1992.1564

[28] J. Zhao, L. Sun, P. Ji, X. Yu, L. Chen, S. Liu, K. Zheng, F. Yin, The effect of scanning strategies on the microstructure and mechanical properties of M2052 alloy manufactured by selective laser melting, Journal of Materials Research and Technology, 27 (2023) 7084-7093. https://doi.org/10.1016/j.jmrt.2023.11.141

[29] V.G. Efremenko, A.G. Lekatou, Y.G. Chabak, B.V. Efremenko, I. Petryshynets, V.I. Zurnadzhy, S. Emmanouilidou, M. Vojtko, Micromechanical, corrosion and wet sliding wear behaviours of Co-28Cr-6Mo alloy: Wrought vs. LPBF, Materials Today Communications, 35 (2023) 105936. https://doi.org/10.1016/j.mtcomm.2023.105936

[30] J.J. Shi, Z.Q. Zhou, K. Xu, G.Y. Zhou, Z.J. Zhou, C.P.

Li, G.F. Chen, X.G. Lu, G.H. Cao, Effect of heat treatment on microstructure and small punch creep property of selective laser melted Inconel 718 alloy, Materials Science and Engineering: A, 853 (2022) 143748. https://doi.org/10.1016/j.msea.2022.143748

[31] V.K. Singh, D. Sahoo, M. Amirthalingam, S. Karagadde, S.K. Mishra, Dissolution of the Laves phase and δ-precipitate formation mechanism in additively manufactured Inconel 718 during post printing heat treatments, Additive Manufacturing, 81 (2024) 104021. https://doi.org/10.1016/j.addma.2024.104021

[32] N. Li, C. Wang, C. Li, Microstructures and high-temperature mechanical properties of Inconel 718 superalloy fabricated via laser powder bed fusion, Materials, 17 (15) (2024) 3735. https://doi.org/10.3390/ma17153735

[33] M. Sundararaman, P. Mukhopadhyay, S. Banerjee, Precipitation of the δ-Ni_3Nb phase in two nickel base superalloys, Metallurgical Transactions A, 19 (3) (1988) 453-465. https://doi.org/10.1007/BF02649259

[34] K.M. Mantrala, M. Das, V.K. Balla, C.S. Rao, V.V.S. Kesava Rao, Additive manufacturing of Co-Cr-Mo alloy: Influence of heat treatment on microstructure, tribological, and electrochemical properties, Frontiers in Mechanical Engineering, 1 (2015) 1-7. https://doi.org/10.3389/fmech.2015.00002

[35] E. Bettini, C. Leygraf, C. Lin, P. Liu, J. Pan, Influence of grain boundaries on dissolution behavior of a biomedical CoCrMo alloy: In-situ electrochemical-optical, AFM and SEM/TEM studies, Journal of The Electrochemical Society, 159 (9) (2012) C422-C427. https://doi.org/10.1149/2.056209jes

[36] T.-N. Lam, K.-M. Chen, C.-H. Tsai, P.-I. Tsai, M.-H. Wu, C.-C. Hsu, J. Jain, E. W. Huang, Effect of porosity and heat treatment on mechanical properties of additive manufactured CoCrMo Alloys, Materials, 16 (2) (2023) 751. https://doi.org/10.3390/ma16020751

[37] M. Roudnicka, J. Bigas, O. Molnarova, D. Palousek, D. Vojtech, Different response of cast and 3D-printed Co-Cr-Mo alloy to heat treatment: A thorough microstructure characterization, Metals, 11 (5) (2021) 687. https://doi.org/10.3390/met11050687

[38] Y. Wang, J. Shi, Recrystallization behavior and tensile properties of laser metal deposited Inconel 718 upon in-situ ultrasonic impact peening and heat treatment, Materials Science and Engineering: A, 786 (2020) 139434. https://doi.org/10.1016/j.msea.2020.139434

[39] L. Zhu, Z. Xu, Y. Gu, Effect of laser power on the microstructure and mechanical properties of heat treated Inconel 718 superalloy by laser solid forming, Journal of Alloys and Compounds, 746 (2018) 159-167. https://doi.org/10.1016/j.jallcom.2018.02.268

[40] Q. Zhi, J. Niu, X. Tan, R. Pei, Y. Liu, Y. Chen, W. Liu, Effect of scanning process and heat treatment on microstructure and mechanical property of Inconel 718 fabricated by selective laser melting, Journal of Materials Engineering and Performance, 32 (21) (2023) 9515-9524. https://doi.org/10.1007/s11665-023-07828-2

[41] W. Huang, J. Yang, H. Yang, G. Jing, Z. Wang, X. Zeng, Heat treatment of Inconel 718 produced by selective laser melting: Microstructure and mechanical properties, Materials Science and Engineering: A, 750 (2019) 98-107. https://doi.org/10.1016/j.msea.2019.02.046

[42] N.Y.S. Tham, G.R.S. Tay, B. Yao, K. Wu, Z. Dong, Effect of aging parameters on Inconel 718 fabricated by laser directed energy deposition, Chinese Journal of Mechanical Engineering: Additive Manufacturing Frontiers, 2 (4) (2023) 100101. https://doi.org/10.1016/j.cjmeam.2023.100101

[43] G.A. Rao, M. Kumar, M. Srinivas, D.S. Sarma, Effect of standard heat treatment on the microstructure and mechanical properties of hot isostatically pressed superalloy inconel 718, Materials Science and Engineering: A, 355 (1) (2003) 114-125. https://doi.org/10.1016/S0921-5093(03)00079-0

[44] L. Huang, Y. Cao, J. Zhang, X. Gao, G. Li, Y. Wang, Effect of heat treatment on the microstructure evolution and mechanical behaviour of a selective laser melted Inconel 718 alloy, Journal of Alloys and Compounds, 865 (2021) 158613. https://doi.org/10.1016/j.jallcom.2021.158613

[45] ASM Handbook Committee, ASM Handbook: Heat Treating, Vol. 4, ASM International, Materials Park, 1991, p. 1795.

[46] C. Slama, M. Abdellaoui, Structural characterization of the aged Inconel 718, Journal of Alloys and Compounds, 306 (1) (2000) 277-284. https://doi.org/10.1016/S0925-8388(00)00789-1

[47] J. Huang, Z. Huang, H. Du, J. Zhang, Effect of aging temperature on microstructure and tensile properties of Inconel 718 fabricated by selective laser melting, Transactions of the Indian Institute of Metals, 75 (6) (2022) 1403-1410. https://doi.org/10.1007/s12666-021-02487-0

[48] Z. Guoqing, L. Junxin, Z. Xiaoyu, L. Jin, W. Anmin, Effect of heat treatment on the properties of CoCrMo alloy manufactured by selective laser melting, Journal of Materials Engineering and Performance, 27 (5) (2018) 2281-2287. https://doi.org/10.1007/s11665-018-3351-5

[49] A.D.J. Saldívar García, A.M. Medrano, A.S. Rodríguez, Formation of hcp martensite during the isothermal aging of an fcc Co-27Cr-5Mo-0.05C orthopedic implant alloy, Metallurgical and Materials Transactions A, 30 (5) (1999) 1177-1184. https://doi.org/10.1007/s11661-999-0267-6

[50] Y. Koizumi, S. Suzuki, K. Yamanaka, B.-S. Lee, K. Sato, Y. Li, S. Kurosu, H. Matsumoto, A. Chiba, Strain-induced martensitic transformation near twin boundaries in a biomedical Co–Cr–Mo alloy with negative stacking fault energy, Acta Materialia, 61 (5) (2013) 1648-1661. https://doi.org/10.1016/j.actamat.2012.11.041

[51] Y. Zhang, W. Lin, Z. Zhai, Y. Wu, R. Yang, Z. Zhang, Enhancing the mechanical property of laser powder bed fusion CoCrMo alloy by tailoring the microstructure and phase constituent, Materials Science and Engineering: A, 862 (2023) 144449. https://doi.org/10.1016/j.msea.2022.144449

[52] X.P. Tan, P. Wang, Y. Kok, W.Q. Toh, Z. Sun, S.M.L. Nai, M. Descoins, D. Mangelinck, E. Liu, S.B. Tor, Carbide precipitation characteristics in additive manufacturing of Co-Cr-Mo alloy via selective electron beam melting, Scripta Materialia, 143 (2018) 117-121. https://doi.org/10.1016/j.scriptamat.2017.09.022

[53] T. Kilner, R.M. Pilliar, G.C. Weatherly, C. Allibert, Phase identification and incipient melting in a cast Co-Cr surgical implant alloy, Journal of Biomedical

Materials Research, 16 (1) (1982) 63-79. https://doi.org/10.1002/jbm.820160109

[54] M. Caudillo, M. Herrera–Trejo, M.R. Castro, E. Ramírez, C.R. González, J.I. Juárez, On carbide dissolution in an as-cast ASTM F-75 alloy, Journal of Biomedical Materials Research, 59 (2) (2002) 378-385. https://doi.org/10.1002/jbm.10001

[55] F.Z. Hassani, M. Ketabchi, S. Bruschi, A. Ghiotti, Effects of carbide precipitation on the microstructural and tribological properties of Co–Cr–Mo–C medical implants after thermal treatment, Journal of Materials Science, 51 (9) (2016) 4495-4508. https://doi.org/10.1007/s10853-016-9762-5

[56] I. Milošev, H.H. Strehblow, The composition of the surface passive film formed on CoCrMo alloy in simulated physiological solution, Electrochimica Acta, 48 (19) (2003) 2767-2774. https://doi.org/10.1016/S0013-4686(03)00396-7

[57] B. Patel, G. Favaro, F. Inam, M.J. Reece, A. Angadji, W. Bonfield, J. Huang, M. Edirisinghe, Cobalt-based orthopaedic alloys: Relationship between forming route, microstructure and tribological performance, Materials Science and Engineering: C, 32 (5) (2012) 1222-1229. https://doi.org/10.1016/j.msec.2012.03.012

[58] J.H. Hollomon, Tensile deformation, Transactions of the Metallurgical Society of AIME, 162 (1945) 268-290.

[59] M. Zubair, S. Sandlöbes, M.A. Wollenweber, C.F. Kusche, W. Hildebrandt, C. Broeckmann, S. Korte-Kerzel, On the role of Laves phases on the mechanical properties of Mg-Al-Ca alloys, Materials Science and Engineering: A, 756 (2019) 272-283. https://doi.org/10.1016/j.msea.2019.04.048

[60] M. Zubair, S. Sandlöbes-Haut, M.A. Wollenweber, K. Bugelnig, C.F. Kusche, G. Requena, S. Korte-Kerzel, Strain heterogeneity and micro-damage nucleation under tensile stresses in an Mg–5Al–3Ca alloy with an intermetallic skeleton, Materials Science and Engineering: A, 767 (2019) 138414. https://doi.org/10.1016/j.msea.2019.138414

[61] D. Yan, C.C. Tasan, D. Raabe, High resolution in situ mapping of microstrain and microstructure evolution reveals damage resistance criteria in dual phase steels, Acta Materialia, 96 (2015) 399-409. https://doi.org/10.1016/j.actamat.2015.05.038

[62] T.R. Bieler, M.A. Crimp, Y. Yang, L. Wang, P. Eisenlohr, D.E. Mason, W. Liu, G.E. Ice, Strain heterogeneity and damage nucleation at grain boundaries during monotonic deformation in commercial purity titanium, JOM, 61 (12) (2009) 45-52. https://doi.org/10.1007/s11837-009-0180-x

[63] A. Dutta, D. Ponge, S. Sandlöbes, D. Raabe, Strain partitioning and strain localization in medium manganese steels measured by in situ microscopic digital image correlation, Materialia, 5 (2019) 100252. https://doi.org/10.1016/j.mtla.2019.100252

[64] G. Zhu, L. Wang, J. Wang, J. Wang, J.-S. Park, X. Zeng, Highly deformable Mg–Al–Ca alloy with Al_2Ca precipitates, Acta Materialia, 200 (2020) 236-245. https://doi.org/10.1016/j.actamat.2020.09.006

KOMPARATIVNA STUDIJA MEHANIČKOG PONAŠANJA TERMIČKI OBRAĐENIH 3D ŠTAMPANIH LEGURA IN-718 I ASTM F75 NA RAZLIČITIM NIVOIMA POSMATRANJA

Muhammad Zubair [a,*], Khushnuda Nur [a], Ehsan Ul Haq [a], Furqan Ahmed [a,], Muhammad Adil Javed[b], Muhammad Junaid Khan [a], Muhammad Mubeen Naveed [a], Mirza Mueed ul Hassan [a], Ahmed Abdullah [a]**

[a] Odsek za metalurško i materijalno inženjerstvo, Fakultet hemijskog, metalurškog i polimernog inženjerstva, Univerzitet za inženjerstvo i tehnologiju (UET), Lahor, Pakistan.
[b] IMMESNA, Dubai, UAE

Apstrakt

Tvrdoća i čvrstoća mnogih legura često se razlikuju kada se mere na nano-, mikro- i makroskopskom nivou. Zbog toga je od suštinskog značaja proučavanje mehaničkog ponašanja važnih legura na širokom opsegu strukturnih nivoa. U ovom radu predstavljen je slučaj u kojem dve industrijski značajne legure, In-718 i ASTM F75, pokazuju različito ponašanje na mikro- i makroskopskom nivou. Obe legure predstavljaju perspektivne materijale za slične primene u vazduhoplovnoj i naftnoj industriji. Legure su najpre proizvedene 3D štampom primenom selektivnog laserskog topljenja (SLM), a zatim termički obrađene u vakuumu. Prosečna granica razvlačenja i procenat izduženja (u pravcu izrade) legure In-718 bili su za 29% i 19% viši, respektivno, u odnosu na vrednosti dobijene za leguru ASTM F75. Razlika između zatezne čvrstoće (UTS) i Vikersove tvrdoće (pri opterećenju od 98 N) bila je gotovo zanemarljiva, odnosno manja od 5%. Nasuprot vrednostima Vikersove tvrdoće od 3,9 GPa i 3,8 GPa, prosečna nanotvrdoća legura In-718 i ASTM F75 iznosila je 5,7 GPa, odnosno 7,6 GPa, što je značajno više od njihovih vrednosti Vikersove tvrdoće. Pored toga, legura ASTM F75 pokazala je znatno bolju otpornost na habanje u ScanningWear ispitivanjima sprovedenim pomoću nanoindentera. U radu su predstavljena objašnjenja ovih razlika, kao i sličnosti između makro- i nanomehaničkog ponašanja ispitivanih legura.

Ključne reči: *Mehanička svojstva; Nanoindentacija; Mehaničko ponašanje; Legure*